Turkish Journal of Chemistry

http://journals.tubitak.gov.tr/chem/

Research Article

Turk J Chem
(2025) 49: 68-78
© TÜBİTAK
doi:10.55730/1300-0527.3711

Preparation and characterization of RhFe/g-C_3N_4 nanoparticles for efficient hydrolysis of sodium borohydride

Merve UÇAR KAYA[1], **Mehmet YURDERİ**[2,3,*], **Mehmet ZAHMAKIRAN**[4]
[1]Department of Metallurgical and Materials Engineering, Faculty of Engineering, Architecture and Design, University of Bartın, Bartın, Turkiye
[2]Department of Electronics and Automation, Bartın Vocational School, University of Bartın, Bartın, Turkiye
[3]Central Research Laboratory, Research & Application Center, NanoMatCat Research Laboratory, University of Bartın,Bartın, Turkiye
[4]Department of Biotechnology, Faculty of Science, Bartın University, Bartın, Turkiye

Received: 06.09.2024 • **Accepted/Published Online:** 11.12.2024 • **Final Version:** 17.02.2025

Abstract: Highly effective graphitic carbon nitride-supported RhFe nanoparticles (RhFe/g-C_3N_4) were prepared using a simple wet impregnation-reduction method for the hydrolysis of sodium borohydride ($NaBH_4$). The obtained $Rh_{0.48}Fe_{0.52}$/g-C_3N_4 catalyst was characterized using advanced analytical/spectroscopic techniques such as inductively coupled plasma-optical emission spectroscopy, scanning electron microscopy, transmission electron microscopy, powder X-ray diffraction, X-ray spectroscopy, and Fourier transform infrared spectroscopy. The catalytic activities of RhFe/g-C_3N_4 catalysts with varying Rh/Fe molar ratios were investigated, demonstrating superior catalytic activity compared to monometallic Rh and Fe. The initial turnover frequency value of the $Rh_{0.48}Fe_{0.52}$/g-C_3N_4 catalyst was calculated as 33.04 min^{-1} and it showed an H_2 generation rate of 4214.02 $\mathrm{mL\ min^{-1}\ g_{cat}^{-1}}$ at 298 K. Furthermore, the kinetic parameters ($E_a^{\#}$, $\Delta H^{\#}$, $\Delta S^{\#}$) of the hydrolysis of $NaBH_4$ catalyzed by the $Rh_{0.48}Fe_{0.52}$/g-C_3N_4 catalyst were elucidated. The findings demonstrated that the resulting $Rh_{0.48}Fe_{0.52}$/g-C_3N_4 catalyst was recyclable and retained 80.72% of the initial activity even after 10 runs.

Key words: Sodium borohydride, hydrolysis, graphitic carbon nitride, catalyst, rhodium, iron

1. Introduction

One of the scenarios for reducing carbon dioxide (CO_2) emissions, which contribute to climate change due to fossil fuel consumption, involves using renewable energy and transitioning to a hydrogen economy without carbon emissions. The challenges of this transition include storage and security concerns [1,2]. Among these, boron compounds are promising solid hydrogen (H_2) storage materials that are widely studied in academia for H_2 production [3,4]. Sodium borohydride ($NaBH_4$) has garnered considerable interest from researchers as a solid hydrogen storage material due to its notable attributes, including a sizable theoretical gravimetric H_2 storage capacity of 10.8 wt% (or volumetric H_2 storage capacity of 115 kg m^{-3}), cost-effectiveness, nontoxicity, stability, nonflammability, favorable reaction conditions, ease of storage, and environmentally friendly byproducts upon release [5,6]. Conventional methods for releasing the H_2 stored in $NaBH_4$ include pyrolysis and hydrolysis. Generally, pyrolysis requires a high temperature (~400 °C), leading to high energy consumption unsuitable for practical applications. However, with suitable catalysts, the hydrolysis of $NaBH_4$ easily releases 4 moles of H_2, even at room temperature Eq. (1) [5,7,8]:

$$\mathrm{NaBH_4 + 2H_2O \rightarrow NaBO_2(aq)\ +\ 4H_2} \tag{1}$$

A low-cost catalyst with high catalytic efficiency and stability is vital in practical fuel cell applications. Recent research has focused on developing bimetallic catalysts incorporating cheaper, abundant first-row transition metals to reduce the consumption of expensive precious metals. Employing nonprecious metals to prepare bimetallic catalysts reduces the cost and secondary precious metal content [9–11]. These bimetallic catalysts often exhibit enhanced catalytic efficiency compared to monometallic catalysts due to synergistic effects [12,13].

The nanoparticles (NPs) in the catalyst tend to aggregate into larger particles, blocking active sites and reducing catalytic performance, especially during recyclability tests. Therefore, solid support materials are essential to prevent active site blockage and metal leaching. In heterogeneous catalysis, the interaction between metal NPs and

---

[*] Correspondence: myurderi@bartin.edu.tr

support materials positively enhances the catalyst's performance [14–17]. Graphitic carbon nitride (g-C_3N_4), a two-dimensional (2D), metal-free organic polymer material, can be easily prepared via pyrolysis reaction and emerges as an interesting solid support material for stabilizing NPs. To the best of our knowledge, g-C_3N_4 is used in many application areas, such as H_2 production [18], pollutant degradation [19], water splitting [20], and hydrogen peroxide production [21], owing to its affordability, environmental friendliness, and unique physicochemical and structural properties [22,23]. Therefore, substantial effort is required to investigate the utilization of g-C_3N_4 as a solid support material.

The motivation herein was to develop stable and efficient bimetallic catalysts for $NaBH_4$ hydrolysis, combining precious metals such as Pt, Ru, and Rh with nonprecious metals like Ni, Co, Cu, and Fe. Hence, this study presents g-C_3N_4-supported rhodium/iron (RhFe) (RhFe/g-C_3N_4) NPs via the impregnation-reduction method and H_2 production in the hydrolysis of $NaBH_4$ at 298 K. Moreover, the obtained catalyst was characterized by advanced analytical methods like inductively coupled plasma-optical emission spectroscopy (ICP-OES), scanning electron microscopy (SEM), electron microscopy (TEM), powder X-ray diffraction (P-XRD), X-ray spectroscopy (XPS), and Fourier transform infrared spectroscopy (FTIR).

2. Materials and methods

2.1. Chemicals

The rhodium(III) chloride hydrate ($RhCl_3{\cdot}xH_2O$, trace metals basis, 99.95%), sodium borohydride $NaBH_4$, (ReagentPlus, 99%), iron(III) chloride hexahydrate ($FeCl_3{\cdot}6H_2O$, American Chemical Society (ACS) reagent, 97%), hydrochloric acid (HCI, ACS reagent, 37%), sodium hydroxide (NaOH, ACS reagent, ≥97.0%), urea (CH_4N_2O, ACS reagent, 99.0%–100.5%), and Whatman qualitative filter paper (Grade 5, diameter: 110 mm) were all purchased from Sigma-Aldrich (Sigma-Aldrich Chemical Co., St. Louis, MO, USA).

2.2. Characterization

The content of the elements in the catalyst was measured using an Optima 4300DV ICP-OES (PerkinElmer Inc., Waltham, MA, USA). SEM images were acquired by a Tescan MAIA3 XMU microscope (Tescan, Brno, Kohoutovice, Czech Republic). The surface morphology and particle size analysis of the catalyst were characterized by TEM (Jeol-2100F; Jeol Ltd., Akishima, Tokyo, Japan) at an accelerating voltage of 200 kV. P-XRD patterns were recorded using a SmartLab X-ray diffractometer (Rigaku Corp., Tokyo, Japan) with Cu K_α radiation (λ = 1.5418 Å) operating at 40 kV and 55 mA. The surface composition and chemical states of the catalyst components were measured using an ESCA-LAB 250xi XPS (Thermo Fisher Scientific Inc., Waltham, MA, USA) equipped with an Al K_α X-ray excitation source. FTIR was performed using a Shimadzu IRTracer-100 spectrometer (Shimadzu Corp., Kyoto, Japan).

2.3. Synthesis of the g-C_3N_4

The g-C_3N_4 synthesis was carried out according to the method in the literature [24]. The starting material, urea (CH_4N_2O), was put into a high-quality alumina crucible and placed in a muffle furnace. Then, the muffle furnace was heated at a rate of 2 °C/min, and the sample was kept at 550 °C for 3 h. After cooling to room temperature, the obtained yellow powder was stored in a desiccator, to be used in the catalytic studies.

2.4. Preparation of the RhFe/g-C_3N_4 NPs

First, 150 mg of g-C_3N_4 was added to 10 mL of H_2O and ultrasonicated for 15 min to form a well-dispersed suspension. Then, $RhCl_3{\cdot}xH_2O$ (0.015 mmol) and $FeCl_3{\cdot}6H_2O$ (0.014 mmol) aqueous solution were added, and the mixture was stirred with a magnetic stirrer at 700 rpm for 3 h. Next, $NaBH_4$ (0.49 mmol) was added dropwise to the mixed solution at the molar ratio metal(s): $NaBH_4$ = 1:15. The final mixture was washed with water/ethanol and filtered with Whatman No. 5 filter paper. The obtained sample was dried in an oven at 80 °C for 1 h. The dried sample was then stored in a desiccator for use in the catalytic experiment.

2.5. Catalytic hydrolysis of $NaBH_4$ catalyzed by RhFe/g-C_3N_4

First, 50.0 mg of the RhFe/g-C_3N_4 catalyst was added to 4.0 mL of deionized water in a 30-mL jacketed Schlenk flask and placed in a thermostat water bath. The mixture was then stirred at 700 rpm and maintained at the desired temperature for 15 min to reach thermal equilibrium. Subsequently, the jacketed Schlenk flask was sealed with an airtight septum to initiate the reaction, followed by injecting 1.0 mL of $NaBH_4$ solution (1 mmol) into the system using an airtight syringe. The volume of H_2 released during the catalytic hydrolysis of $NaBH_4$ catalyzed by the RhFe/g-C_3N_4 catalyst was monitored by measuring the water-displacement method in a 200-cm^3 gas burette [25–27]. Upon completion of the $NaBH_4$ hydrolysis, the recorded gas volume (in mL) over time was imported into Origin 10.1 software (OriginLab Corp., Northampton, MA, USA) to generate corresponding graphs.

3. Results

The g-C_3N_4 was synthesized by keeping the starting material (urea, CH_4N_2O) in a muffle furnace at 550 °C for 3 h. Then, RhFe NPs were decorated on the g-C_3N_4 surface using the impregnation-reduction method following a previously reported procedure. The RhFe/g-C_3N_4 bimetallic catalyst was obtained as dark gray powder and determined using ICP-OES, SEM, TEM, P-XRD, XPS, and FTIR analyses.

ICP-OES analysis was used to determine the elemental composition of the RhFe/g-C_3N_4 catalyst. The molar composition of the Rh and Fe in the prepared RhFe/g-C_3N_4 catalyst was $Rh_{0.48}Fe_{0.52}$/g-C_3N_4 (0.38% wt Rh and 0.54% wt Fe). P-XRD analysis of the crystal and phase structures of the g-C_3N_4 and g-C_3N_4-supported $Rh_{0.48}Fe_{0.52}$ NPs are given in Figure 1. The Bragg diffraction peaks located at 12.96° (weak, corresponding to the in-plane structural motif of tris-triazine units) and 27.60° (strong, belonging to the interlayer stacking of the C_3N_4 layered structure) were attributed to the (100) and (002) crystal planes of the g-C_3N_4, respectively. These two Bragg diffraction peaks were consistent with g-C_3N_4, as reported in the literature [28,29]. The P-XRD pattern in Figure 1 shows that the crystal structure of the g-C_3N_4 in the $Rh_{0.48}Fe_{0.52}$/g-C_3N_4 catalyst was not affected by the decoration of the $Rh_{0.48}Fe_{0.52}$ NPs. Moreover, the Bragg diffraction peaks in the P-XRD corresponding to the $Rh_{0.48}Fe_{0.52}$ NPs could not be observed due to the low content of the $Rh_{0.48}Fe_{0.52}$ NPs (<5 wt%) and the good dispersion [30].

The SEM images (Figures 2a–2c) and their elemental composition mapping were used to analyze the provided information regarding the surface topography of the catalyst. The elemental mapping given in Figures 2d–2h shows that the Rh, Fe, C, and N in the $Rh_{0.48}Fe_{0.52}$/g-C_3N_4 catalyst were distributed homogeneously without any accumulation. Moreover, the SEM-EDX spectrum taken from a certain area confirmed the existence of the four elements (Figure 2i).

At the same time, TEM analysis was used to determine the distribution and size of the NPs. Based on the TEM image (Figure 3) analysis conducted using ImageJ (US National Institutes of Health, Bethesda, MD, USA), the sample revealed approximately >94 RhFe NPs decorated on the g-C_3N_4 surface. The analysis further yielded an average particle size of 2.68 ± 0.63 nm (inset, Figure 3), indicating a uniform distribution of RhFe NPs with a relatively small size.

FTIR analysis was used to investigate the chemical bonding structures of the g-C_3N_4 and $Rh_{0.48}Fe_{0.52}$/g-C_3N_4 samples (Figure 4). The characteristic peaks detected at approximately 1232, 1313, 1402, 1535, and 1631 cm^{-1} corresponded to the vibrations of C–N [31,32]. The peak at 808 cm^{-1} belonged to the individual breathing mode of triazine rings [33]. Moreover, the broad bands at 3082–3296 cm^{-1} were attributed to N–H and O–H stretching vibration modes [34,35]. Furthermore, the structure of the g-C_3N_4 was not affected due to the decoration of the $Rh_{0.48}Fe_{0.52}$ NPs.

XPS analysis was conducted to elucidate the composition and chemical state of the $Rh_{0.48}Fe_{0.52}$/g-C_3N_4 catalyst. As depicted in Figure 5a, the surface XPS spectrum exhibited signals attributed to Rh, Fe, C, N, and O, affirming the successful attachment of Rh and Fe to the g-C_3N_4 surface. In the high-resolution (HR) Rh 3d XPS spectrum given in Figure 5b, the two central peaks at 307.27 and 312.58 eV are the Rh $3d_{5/2}$ and Rh $3d_{3/2}$ peaks of Rh(0), respectively [36]. The HR Fe 2p core-level spectrum of the Fe $2p_{3/2}$ exhibits two peaks at 709.0 and 722.2 eV associated with the Fe $2p_{3/2}$ and Fe $2p_{1/2}$ peak of Fe(0) for $Rh_{0.48}Fe_{0.52}$/g-C_3N_4 (Figure 5c) [37,38]. The binding energies of Fe(0) $2p_{3/2}$ and Fe(0) $2p_{1/2}$ for the $Rh_{0.48}Fe_{0.52}$/g-C_3N_4 exhibit an upshift of ~0.64 eV compared to $Fe_{1.0}$/g-C_3N_4. This indicates that there was electron transfer between the

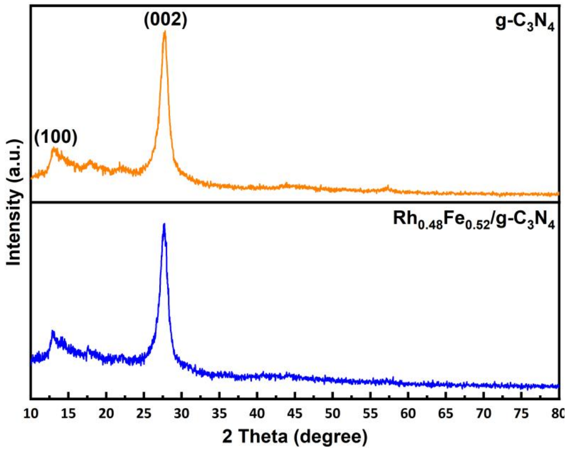

Figure 1. P-XRD spectra of the g-C_3N_4 and $Rh_{0.48}Fe_{0.52}$/g-C_3N_4 catalyst in the range of 2θ° of 10–80°.

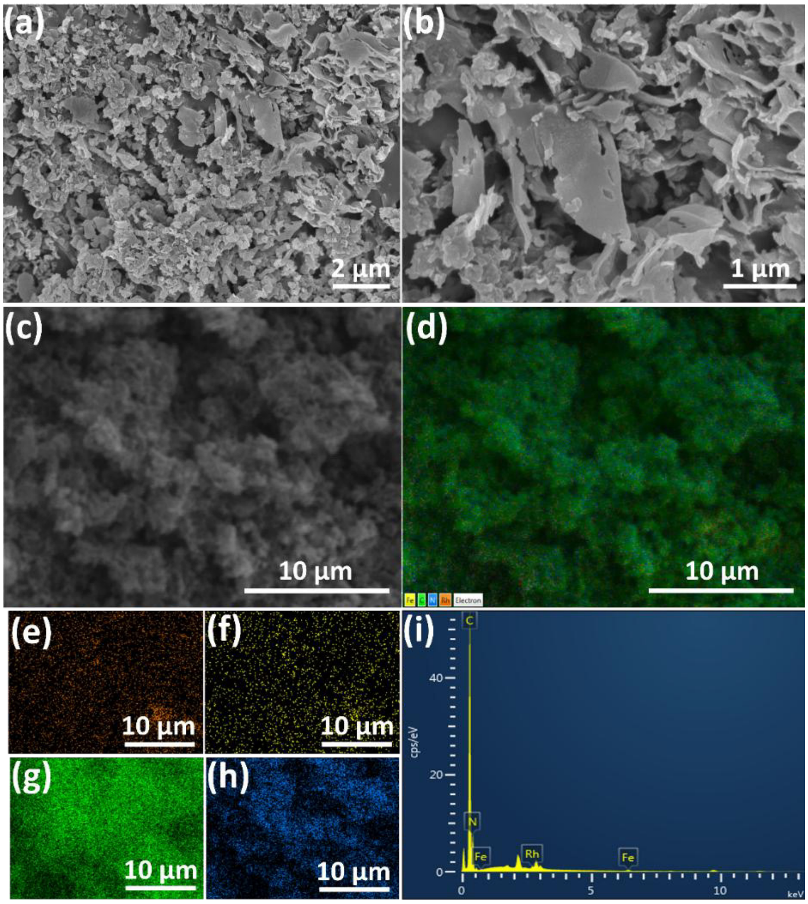

Figure 2. (a–c) SEM images, (d) combined (Rh, Fe, C, and N), (e) Rh, (f) Fe, (g) C, (h) N EDX elemental mapping, and (i) EDX spectrum of the $Rh_{0.48}Fe_{0.52}/g\text{-}C_3N_4$.

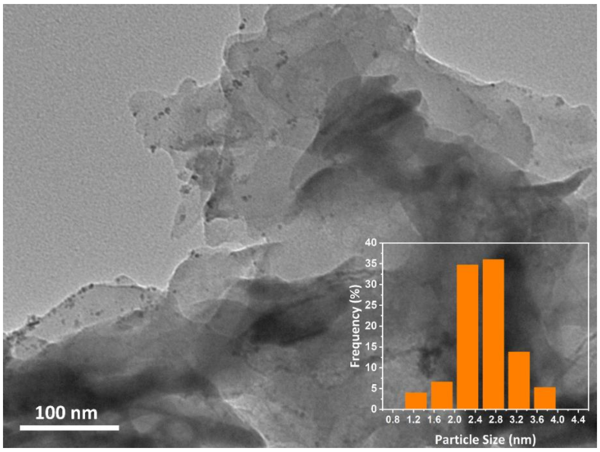

Figure 3. TEM image and average particle size histogram of the $Rh_{0.48}Fe_{0.52}/g\text{-}C_3N_4$.

Rh and Fe. This can be corroborated by examining Figure 6. The catalysts consisting of only $Rh_{1.0}/g\text{-}C_3N_4$ and $Fe_{1.0}/g\text{-}C_3N_4$ had much lower catalytic activities toward $NaBH_4$ hydrolysis. However, the $Rh_{0.48}Fe_{0.52}/g\text{-}C_3N_4$ bimetallic catalyst had much better catalytic activity.

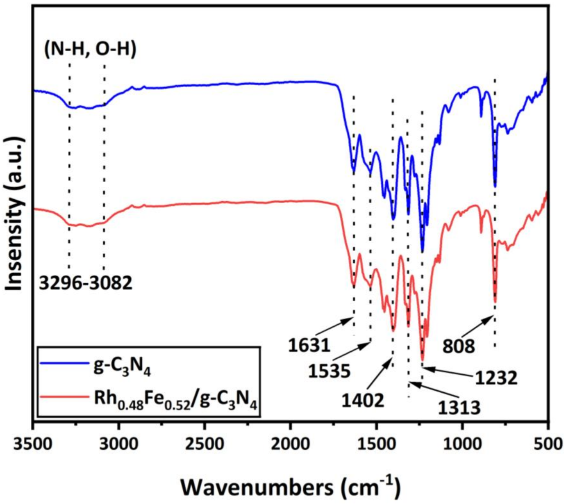

Figure 4. FTIR spectra of the g-C_3N_4 and $Rh_{0.48}Fe_{0.52}$/g-C_3N_4 catalyst.

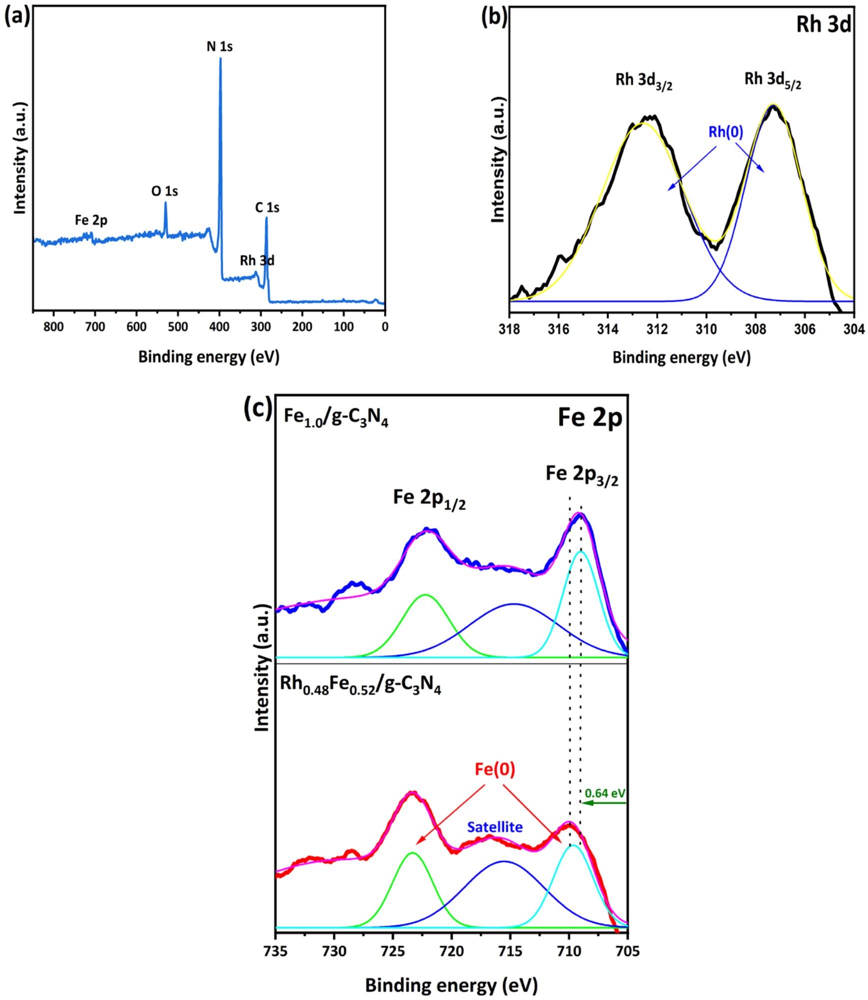

Figure 5. (a) XPS surface and HR XPS spectra of (b) Rh 3d and (c) Fe 2p for the $Rh_{0.48}Fe_{0.52}$/g-C_3N_4 catalyst.

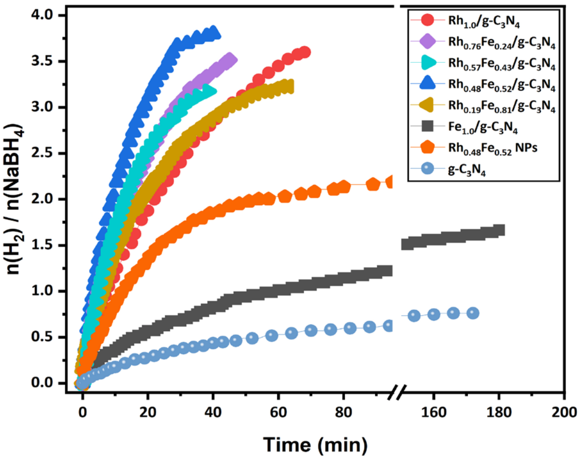

Figure 6. H_2 produced kinetics curves of the different mono and bimetallic catalysts for the hydrolysis of $NaBH_4$ at 298 K.

The molar metal composition (Rh/Fe) impacted the performance of RhFe/g-C_3N_4 in the hydrolysis of $NaBH_4$. H_2 production via the hydrolysis of $NaBH_4$ was evaluated using mono/bimetallic catalysts ($Rh_{1.0}$/g-C_3N_4, $Fe_{1.0}$/g-C_3N_4, Rh_xFe_{1-x}/g-C_3N_4) prepared in $NaBH_4$ aqueous solution at 298 K. Figure 6 shows the time-dependent H_2 evaluation graph in $NaBH_4$ hydrolysis catalyzed by RhFe/g-C_3N_4 catalysts with different Rh/Fe molar ratios. The graph shows that the $Rh_{1.0}$/g-C_3N_4 and $Fe_{1.0}$/g-C_3N_4 catalysts produce 3.6 moles of H_2 in 68 min and 1.66 moles of H_2 in 180 min in the $NaBH_4$ hydrolysis, which indicates that the Rh/g-C_3N_4 and Fe/g-C_3N_4 catalysts alone could not release 4 moles of H_2 from $NaBH_4$ hydrolysis. As the molar ratio between the Rh and Fe in the Rh_xFe_{1-x}/g-C_3N_4 catalyst changed, the catalytic efficiency in the $NaBH_4$ hydrolysis increased. The catalytic activities obtained in the bimetallic $Rh_{0.48}Fe_{0.52}$/g-C_3N_4 catalysts were compared to the monometallic $Rh_{1.0}$/g-C_3N_4 and $Fe_{1.0}$/g-C_3N_4 catalysts in terms of the initial turnover frequency (TOF) values. Among the bimetallic catalysts in the graph, the optimized $Rh_{0.48}Fe_{0.52}$/g-C_3N_4 catalyst provided the highest activity in the hydrolysis of $NaBH_4$, with an initial TOF value of 33.04 $\mathrm{mol_{H_2}\ mol_{metal}^{-1}\ min^{-1}}$ and produced ~3.9 moles of H_2 in 40 min. Moreover, the $Rh_{0.48}Fe_{0.52}$/g-C_3N_4 catalyst exhibited a TOF value of 33.04 $\mathrm{mol_{H_2}\ mol_{metal}^{-1}\ min^{-1}}$, which was higher than those of the $Rh_{1.0}$/g-C_3N_4 (18.21 $\mathrm{mol_{H_2}\ mol_{metal}^{-1}\ min^{-1}}$), $Fe_{1.0}$/g-C_3N_4 (4.93 $\mathrm{mol_{H_2}\ mol_{metal}^{-1}\ min^{-1}}$) and colloidal $Rh_{0.48}Fe_{0.52}$ NPs without g-C_3N_4 (12.62 $\mathrm{mol_{H_2}\ mol_{metal}^{-1}\ min^{-1}}$). The effect of the g-$C_3N_4$ on $NaBH_4$ hydrolysis was also investigated without impregnation of the $Rh_{0.48}Fe_{0.52}$ NPs, and it was observed that g-C_3N_4 exhibited very low catalytic activity compared to the $Rh_{0.48}Fe_{0.52}$/g-C_3N_4 catalyst.

The effect of the amount of [$Rh_{0.48}Fe_{0.52}$] on the hydrolysis of $NaBH_4$ over the $Rh_{0.5}Fe_{0.5}$/g-C_3N_4 catalyst was investigated across amounts of [$Rh_{0.48}Fe_{0.52}$] ranging from 25 to 75 mg ([$NaBH_4$] = 100 mM, 298 K). Figure 7a depicts the volumetric H_2 released over time during hydrolysis of the NaBH4 on the $Rh_{0.48}Fe_{0.52}$/g-C_3N_4 catalyst at varying amounts [$Rh_{0.48}Fe_{0.52}$]. As seen in the graph, the hydrolysis time of $NaBH_4$ increased as the amount of [$Rh_{0.48}Fe_{0.52}$] increased from 25 to 75 mg (25, 37.5, 50, 62.5, and 75.0 mg amount of catalyst correspond to 0.95, 1.42, 1.9, 2.37, and 2.84 mM RhFe concentrations). The H_2 evolution rates for the different amounts of [$Rh_{0.48}Fe_{0.52}$] were determined by examining the linear parts of each plot in Figure 7b. The resulting linear part gave a slope of 0.94, indicating that the catalytic process of $NaBH_4$ hydrolysis by $Rh_{0.48}Fe_{0.52}$/g-C_3N_4 adhered to first-order kinetics. Figure 7c shows the effect of different [$NaBH_4$] concentrations on the hydrolysis of $NaBH_4$ catalyzed by $Rh_{0.48}Fe_{0.52}$/g-C_3N_4 (catalyst = 50 mg, 298 K]). The slope was calculated as 0.06 from the logarithmic graph of H_2 evolution rates obtained from each graph in Figure 7d. This indicates that the hydrolysis of $NaBH_4$ catalyzed by $Rh_{0.48}Fe_{0.52}$/g-C_3N_4 was a zero-order reaction related to the [$NaBH_4$] concentration. The temperature effect on the H_2 evolution rate in the $NaBH_4$ hydrolysis catalyzed by $Rh_{0.48}Fe_{0.52}$/g-C_3N_4 was also examined (catalyst = 50 mg, [$NaBH_4$] = 100 mM).

Figure 8 shows the volumetric H_2 release versus time plot for hydrolysis of the $NaBH_4$ on the $Rh_{0.48}Fe_{0.52}$/g-C_3N_4 catalyst at different temperatures (20, 25, 30, 35, and 40 °C). In the graph, the H_2 evolution rate also increased with temperature, which shows that temperature seriously impacted the H_2 formation rate in hydrolysis of the $NaBH_4$. The activation energy ($E_a^{\#}$) is a critical metric for investigating the catalytic process of $NaBH_4$ hydrolysis. The $E_a^{\#}$ value for the hydrolysis reaction catalyzed by the optimized $Rh_{0.48}Fe_{0.52}$/g-C_3N_4 bimetallic catalyst was determined using the Arrhenius equation. In Figures 8b and 8c, the rate constants calculated from the linear part of each graph were transferred to the Arrhenius and Eyring equations and calculated as $E_a^{\#}$ 66.20 $\mathrm{kJ\ mol^{-1}}$, activation enthalpy ($\Delta H^{\#}$) 63.68 $\mathrm{kJ\ mol^{-1}}$, and activation entropy ($\Delta S^{\#}$) –149.53 $\mathrm{J\ mol^{-1}\ K^{-1}}$.

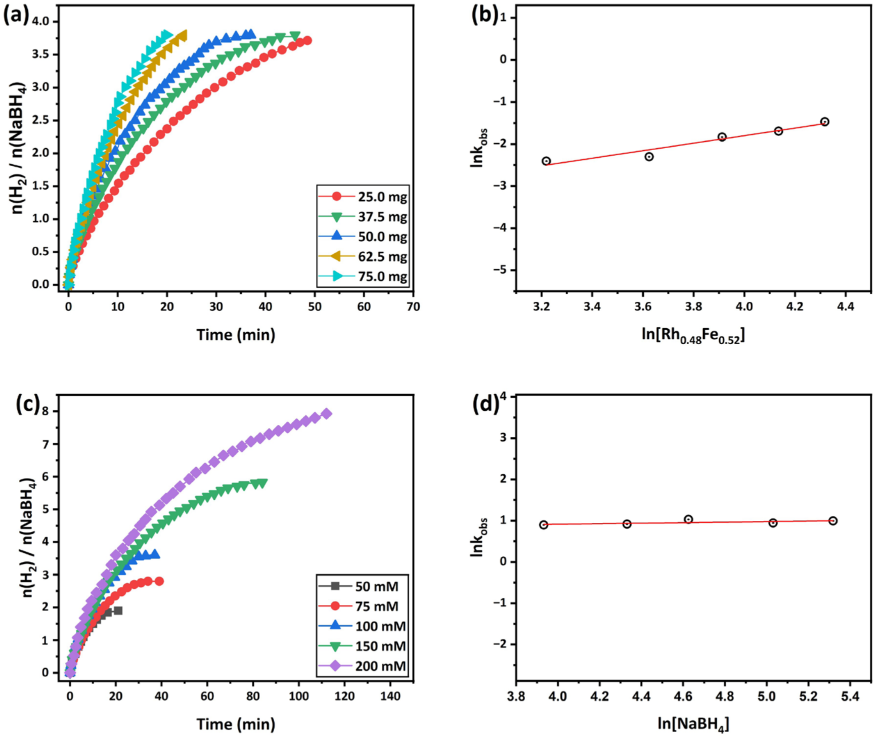

Figure 7. (a) H_2 produced kinetics curves of different catalyst amount for the hydrolysis of $NaBH_4$ catalyzed by the $Rh_{0.48}Fe_{0.52}/g\text{-}C_3N_4$ at 298 K, (b) logarithmic plot of the H_2 produced rate versus the amount of catalyst, (c) H_2 produced kinetics curves of the different $NaBH_4$ concentrations for the hydrolysis of $NaBH_4$ catalyzed by the $Rh_{0.48}Fe_{0.52}/g\text{-}C_3N_4$ at 298 K, and (d) logarithmic plot of the H_2 produced rate versus the $NaBH_4$ concentrations.

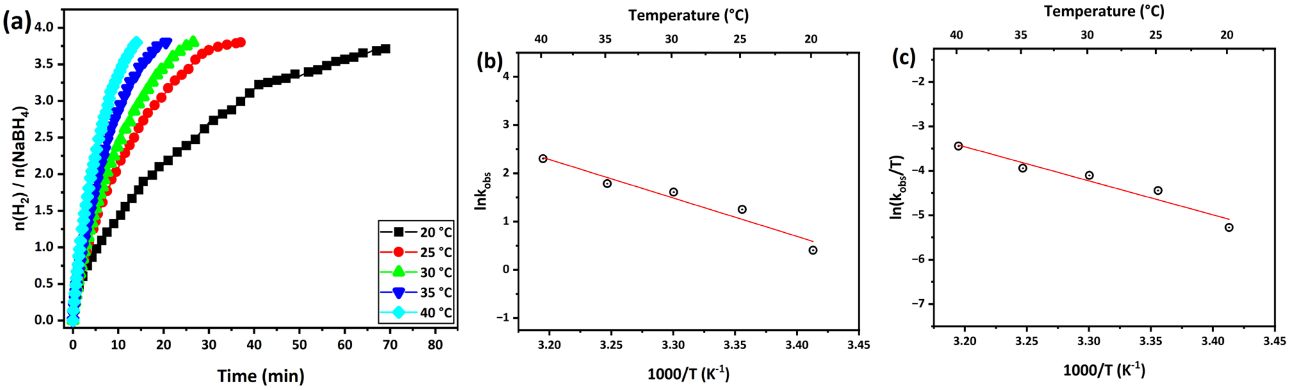

Figure 8. (a) H_2 produced kinetics curves of the different temperatures for the hydrolysis of $NaBH_4$ catalyzed by the $Rh_{0.48}Fe_{0.52}/g\text{-}C_3N_4$, (b) Arrhenius plot, and (c) Eyring-Polanyi plot.

The $Ea^{\#}$ for the $Rh_{0.5}Fe_{0.5}/g\text{-}C_3N_4$ was lower than most of the catalysts reported in Table, indicating that this catalyst can remarkably reduce the energy barrier for $NaBH_4$ hydrolysis, thus facilitating the formation of H_2 from $NaBH_4$ hydrolysis under mild conditions.

Moreover, the stability of the catalyst is significant for use in large-scale industrial production. The recyclability performance of the $Rh_{0.48}Fe_{0.52}/g\text{-}C_3N_4$ catalyst for the hydrolysis of $NaBH_4$ up to the 10th catalytic cycle is given in Figure 9. Following completion of the 1st cycle, fresh $NaBH_4$ solution was added to the reaction medium, and catalytic testing continued through the 10th cycle. The $Rh_{0.48}Fe_{0.52}/g\text{-}C_3N_4$ catalyst catalyzed the hydrolysis of $NaBH_4$ to produce about ~4 equivalent of H_2 per mole of $NaBH_4$. As the number of cycles increased, the conversion time of the $NaBH_4$ also increased

Table. TOF and *Ea*$^{\#}$ values of the catalysts tested in the hydrolysis of $NaBH_4$.

	Catalyst	HGR (mL min^{-1} g_{cat}^{-1})	Ea$^{\#}$ (kJ mol^{-1})	Reference
1	Pd/Co_3O_4	2109	65.82	[39]
2	Fe/SiO_2	130	59	[40]
3	Fe_2O_3@BS	286	39.59	[41]
4	Ru-RuO_2/C	2800	-	[42]
5	$Ru_{4.7}$/Co-Sm_2O_3	9636	53.2	[43]
6	RuCo/C	3420	29.3	[44]
7	Cu-Co-B	2120	49.6	[45]
8	Fe-B	59	64.26	[46]
9	Ru-9.0/ZIF-67	5520	39	[47]
10	Co@NHC	1515.4	14.8	[48]
11	$FeCo_2O_4$/CC	2251	45.0	[49]
12	$FeCuCoO_x$	1380	16.3	[50]
13	**$Rh_{0.48}Fe_{0.52}$/g-C_3N_4**	**4214.02**	**66.20**	**This study**

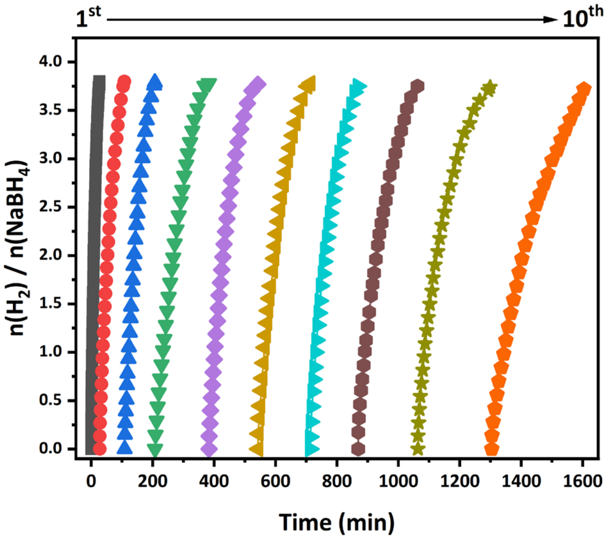

Figure 9. Recyclability performance of the $NaBH_4$ catalyzed by the $Rh_{0.48}Fe_{0.52}$/g-C_3N_4 catalyst up to the 10th cycle at 298 K.

slightly. This indicates a decrease in activity, which caused the accumulation of $NaBO_2$ [51], a byproduct formed in the solution with each addition of $NaBH_4$ to the system. Therefore, this shows that it blocked the catalyst's active sites and prevented contact between the catalyst and the $NaBH_4$ solution.

The P-XRD pattern of the $Rh_{0.48}Fe_{0.52}$/g-C_3N_4 catalyst taken after 10 cycles (Figure 10) was the same as that of the $Rh_{0.48}Fe_{0.52}$/g-C_3N_4, indicating that the crystallinity of the solid support material (g-C_3N_4) was maintained after 10 cycles.

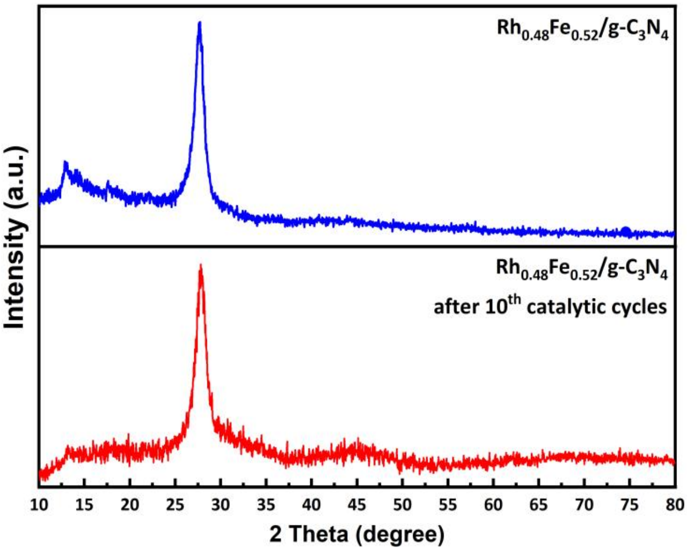

Figure 10. P-XRD spectra of after 10th catalytic cycle for the $Rh_{0.48}Fe_{0.52}/g\text{-}C_3N_4$ and $Rh_{0.48}Fe_{0.52}/g\text{-}C_3N_4$ catalyst in the range of 2θ° of 10–80°.

4. Discussion

The preparation of a $RhFe/g\text{-}C_3N_4$ catalyst via a simple and reproducible impregnation-reduction method in a 4-h procedure was presented. The optimized $Rh_{0.48}Fe_{0.52}/g\text{-}C_3N_4$ catalyst exhibited outstanding performance with an initial TOF of 33.04 $\text{mol}_{H_2}\,\text{mol}^{-1}_{\text{metal}}\text{h}^{-1}$ and an H_2 generation rate (HGR) of 4214.02 mL $\text{min}^{-1}\text{g}^{-1}_{\text{cat}}$ at 298 K. The catalytic activity of the $Rh_{0.48}Fe_{0.52}/g\text{-}C_3N_4$ in the hydrolysis of $NaBH_4$ was evaluated under different temperatures, concentrations of [RhFe NPs] and [$NaBH_4$], and recyclability conditions. The activation parameters ($E_a^{\#}$, $\Delta H^{\#}$, $\Delta S^{\#}$) for hydrolysis of the $NaBH_4$ catalyzed by $Rh_{0.48}Fe_{0.52}/g\text{-}C_3N_4$ were calculated as 66.20 kJ mol^{-1}, 63.68 kJ mol^{-1}, and –149.53 $\text{J mol}^{-1}\text{K}^{-1}$, respectively. Moreover, the resulting $Rh_{0.48}Fe_{0.52}/g\text{-}C_3N_4$ catalyst was recyclable and retained 80.72% of the initial activity even after 10 runs. These findings highlight the potential of $Rh_{0.48}Fe_{0.52}/g\text{-}C_3N_4$ catalysts for efficient H_2 production, paving the way for their application in fuel cell-based H_2 economies.

References

[1] Long B, Chen J, Sharshir SW, Ibrahim L, Zhou W et al. The mechanism and challenges of cobalt-boron-based catalysts in the hydrolysis of sodium borohydride. Journal of Material Chemistry A 2024; 12 (10): 5606-5625. https://doi.org/10.1039/D3TA07308D

[2] Pope F, Jonk J, Fowler M, Lan PCM, Geels NJ et al. From shrimp balls to hydrogen bubbles: borohydride hydrolysis catalysed by flexible cobalt chitosan spheres. Green Chemistry 2023; 25 (14): 5727-5734. https://doi.org/10.1039/D3GC00821E

[3] Netskina OV, Bulakov VE, Sukhorukov DA, Ozerova AM, Prosvirin IP et al. Ferromagnetic "nickel core–cobalt shell" catalysts for $NaBH_4$ hydrolysis. New Journal of Chemistry 2024; 48 (7): 3304-3315. https://doi.org/10.1039/D3NJ04579J

[4] Çetin MB, Top T, Yurderi M, Zahmakıran M, Rakap M. Tungsten(VI) oxide-supported nickel/silver nanoparticles for photocatalytic hydrogen evolution from ammonia-borane. International Journal of Hydrogen Energy 2024; 72: 60-73. https://doi.org/10.1016/j.ijhydene.2024.05.361

[5] Liu X, Sun W, Chen J, Wen Z. Controllable electrochemical liberation of hydrogen from sodium borohydride. Angewandte Chemie International Edition 2024; 136 (4): e202317313. https://doi.org/10.1002/anie.202317313

[6] Ekinci A, Genli N, Şahin Ö, Baytar O. Facile "Green" synthesis of a novel Co–W–B catalyst from Rheum ribes shell extract and its effect on sodium borohydride hydrolysis: Kinetic mechanism. International Journal of Hydrogen Energy 2024; 51: 796-808. https://doi.org/10.1016/j.ijhydene.2023.07.069

[7] Sun Q, Wang N, Xu Q, Yu J. Nanopore-supported metal nanocatalysts for efficient hydrogen generation from liquid-phase chemical hydrogen storage materials. Advanced Materials 2020; 32 (44): 2001818. https://doi.org/10.1002/adma.202001818

[8] Demirci UB, Miele P. Sodium borohydride versus ammonia borane, in hydrogen storage and direct fuel cell applications. Energy & Environmental Science 2009; 2 (6): 627-637. https://doi.org/10.1039/B900595A

[9] Zhang H, Zhang L, Rodríguez-Pérez IA, Miao W, Chen K et al. Carbon nanospheres supported bimetallic Pt-Co as an efficient catalyst for $NaBH_4$ hydrolysis. Applied Surface Science 2021; 540: 148296. https://doi.org/10.1016/j.apsusc.2020.148296

[10] Shang N, Zhou X, Feng C, Gao S, Wu Q et al. Synergetic catalysis of NiPd nanoparticles supported on biomass-derived carbon spheres for hydrogen production from ammonia borane at room temperature. International Journal of Hydrogen Energy 2017; 42 (9): 5733-5740. https://doi.org/10.1016/j.ijhydene.2016.11.192

[11] Al-Thabaiti SA, Khan Z, Malik MA. Bimetallic Ag-Ni nanoparticles as an effective catalyst for hydrogen generation from hydrolysis of sodium borohydride. International Journal of Hydrogen Energy 2019; 44 (31): 16452-16466. https://doi.org/10.1016/j.ijhydene.2019.04.240

[12] Mori K, Miyawaki K, Yamashita H. Ru and Ru-Ni nanoparticles on TiO_2 support as extremely active catalysts for hydrogen production from ammonia-borane. ACS Catalysis 2016; 6 (5): 3128-3135. https://doi.org/10.1021/acscatal.6b00715

[13] Li YT, Zhang XL, Peng ZK, Liu P, Zheng XC. Hierarchical porous g-C_3N_4 coupled ultrafine RuNi alloys as extremely active catalysts for the hydrolytic dehydrogenation of ammonia borane. ACS Sustainable Chemistry & Engineering 2020; 8 (22): 8458-8468. https://doi.org/10.1021/acssuschemeng.0c03009

[14] Pradhan MR, Nanda BB, Subhadarshini A, Panda L, Nanda B. Enhanced catalytic reductive hydrogenation of an organic dye by Ag decorated graphitic carbon nitride modified MCM-41. RSC Advances 2024; 14 (2): 1072-1081. https://doi.org/10.1039/D3RA05608B

[15] Singh Chouhan R, Jerman I, Heath D, Bohm S, Gandhi S et al. Emerging tri-s-triazine-based graphitic carbon nitride: a potential signal-transducing nanostructured material for sensor applications. Nano Select 2021; 2 (4): 712-743. https://doi.org/10.1002/nano.202000228

[16] Niu P, Dai J, Zhi X, Xia Z, Wang S et al. Photocatalytic overall water splitting by graphitic carbon nitride. InfoMat 2021; 3 (9): 931-961. https://doi.org/10.1002/inf2.12219

[17] Idris AO, Oseghe EO, Msagati TAM, Kuvarega AT, Feleni U et al. Graphitic carbon nitride: a highly electroactive nanomaterial for environmental and clinical sensing. Sensors 2020; 20 (20): 5743. https://doi.org/10.3390/s20205743

[18] Zhang Y, Liu D, Shi J, Chen P, Zong S et al. (Oxy)nitride heterojunction-strengthened separation of photogenerated carriers in g-C_3N_4 towards enhanced photocatalytic H_2 evolution. Applied Catalysis A: General 2022; 643: 118746. https://doi.org/10.1016/j.apcata.2022.118746

[19] Li Y, Chen C, Chen X, Zang J. MoO_3/g-C_3N_4 heterostructure for degradation of organic pollutants under visible light irradiation: high efficiency, general degradation and Z-scheme degradation mechanism. Ceramics International 2021; 47 (23): 33697-33708. https://doi.org/10.1016/j.ceramint.2021.08.279

[20] Li Y, Zhu S, Kong X, Liang Y, Li Z et al. In situ synthesis of a novel Mn_3O_4/g-C_3N_4 p-n heterostructure photocatalyst for water splitting. Journal of Colloid and Interface Science 2021; 586: 778-784. https://doi.org/10.1016/j.jcis.2020.11.002

[21] Hu J, Zhang P, Yang T, Cai Y, Qu J et al. Screen superior ultra-thin g-C_3N_4 material for photocatalytic in-situ H_2O_2 production to remove tetracycline. Applied Surface Science 2022; 576: 151841. https://doi.org/10.1016/j.apsusc.2021.151841

[22] Liu S, Liu JX, Yang M, Zhang XL, Zheng XC et al. Ultrafine Pd nanoparticles stabilized on magnetic Fe_3O_4@SiO_2-g-C_3N_4 composites for the hydrolytic dehydrogenation of ammonia borane. International Journal of Hydrogen Energy 2020; 45 (55): 30511-30520. https://doi.org/10.1016/j.ijhydene.2020.08.064

[23] Lu R, Hu M, Xu C, Wang Y, Zhang Y et al. Hydrogen evolution from hydrolysis of ammonia borane catalyzed by Rh/g-C_3N_4 under mild conditions. International Journal of Hydrogen Energy 2018; 43 (14): 7038-7045. https://doi.org/10.1016/j.ijhydene.2018.02.148

[24] Chava RK, Kang M. Ordered and carbon-doped porous polymeric graphitic carbon nitride nanosheets toward enhanced visible light absorption and efficient photocatalytic H_2 evolution. Nanoscale 2023; 15 (45): 18347-18358. https://doi.org/10.1039/D3NR04270G

[25] Xu F, Huang W, Wang Y, Astruc D, Liu X. Efficient and controlled H_2 release from sodium formate. Inorganic Chemistry Frontiers 2022; 9 (14): 3514-3521. https://doi.org/10.1039/D2QI00774F

[26] Li G, Wei N, Wang Y. Active clusters ensemble effect of bimetallic RuCo alloys for efficient hydrogen production from ammonia borane. Applied Surface Science 2023; 610: 155459. https://doi.org/10.1016/j.apsusc.2022.155459

[27] Yılmaz C, Yıldırım HA, Top T, Yurderi M, Zahmakıran M. ZIF-8 decorated FeMo nanoparticles: H_2 production from the catalytic hydrolysis of ammonia-borane. Environmental and Progress & Sustainable Energy 2024; 43 (5): e14439. https://doi.org/10.1002/ep.14439

[28] Ding X, Gao R, Chen Y, Wang H, Liu Y et al. Carbon vacancies in graphitic carbon nitride-driven high catalytic performance of Pd/CN for phenol-selective hydrogenation to cyclohexanone. ACS Catalysis 2024; 14 (5): 3308-3319. https://doi.org/10.1021/acscatal.3c05625

[29] Ismael M. Construction of novel Ru-embedded bulk g-C_3N_4 photocatalysts toward efficient and sustainable photocatalytic hydrogen production. Diamond & Related Materials 2024; 144: 111024. https://doi.org/10.1016/j.diamond.2024.111024

[30] Han C, Lu Y, Zhang J, Ge L, Li Y et al. Novel PtCo alloy nanoparticle decorated 2D g-C_3N_4 nanosheets with enhanced photocatalytic activity for H_2 evolution under visible light irradiation. Journal of Materials Chemistry A 2015; 3 (46): 23274-23282. https://doi.org/10.1039/C5TA05370F

[31] Kim M, Hwang S, Yu JS. Novel ordered nanoporous graphitic C_3N_4 as a support for Pt–Ru anode catalyst in direct methanol fuel cell. Journal of Materials Chemistry 2007; 17 (17): 1656-1659. https://doi.org/10.1039/B702213A

[32] Mo Z, She X, Li Y, Liu L, Huang L et al. Synthesis of g-C_3N_4 at different temperatures for superior visible/UV photocatalytic performance and photoelectrochemical sensing of MB solution. RSC Advances 2015; 5 (123): 101552-101562. https://doi.org/10.1039/C5RA19586A

[33] Thanh Truc NT, Hanh NT, Nguyen MV, Le Chi NTP, Noi NV et al. Novel direct Z-scheme $Cu_2V_2O_7$/g-C_3N_4 for visible light photocatalytic conversion of CO_2 into valuable fuels. Applied Surface Science 2018; 457: 968-974. https://doi.org/10.1016/j.apsusc.2018.07.034

[34] Qi K, Zada A, Yang Y, Chen Q, Khataee A. Design of 2D–2D NiO/g-C_3N_4 heterojunction photocatalysts for degradation of an emerging pollutant. Research on Chemical Intermediates 2020; 46 (12): 5281-5295. https://doi.org/10.1007/s11164-020-04262-0

[35] Narkbuakaew T, Sujaridworakun P. Synthesis of tri-s-triazine based g-C_3N_4 photocatalyst for cationic rhodamine B degradation under visible light. Topics in Catalysis 2020; 63 (11-14): 1086-1096. https://doi.org/10.1007/s11244-020-01375-z

[36] Zhu JY, Li FM, Yao L, Han CC, Li SN et al. In situ bubble template-assisted synthesis of phosphonate-functionalized Rh nanodendrites and their catalytic application. CrystEngComm 2017; 19 (21): 2946-2952. https://doi.org/10.1039/C7CE00606C

[37] Paksoy A, Kurtoğlu-Öztulum SF, Yağcı MB, Balcı-Çağıran Ö. Low-cost and reusable iron- and nickel-based metal boride nanoparticles for efficient catalytic hydrolysis of sodium borohydride. International Journal of Hydrogen Energy 2022; 47 (87): 36898-36913. https://doi.org/10.1016/j.ijhydene.2022.08.269

[38] Guan K, Wang L, Huang L, Lei W, Jia Q et al. Synthesis and high catalytic activity of ISOBAM-104 stabilized Fe colloidal catalysts for hydrogen generation. Catalysis Today 2021; 374: 20-28. https://doi.org/10.1016/j.cattod.2020.10.028

[39] Bozkurt G, Özer A, Yurtcan AB. Development of effective catalysts for hydrogen generation from sodium borohydride: Ru, Pt, Pd nanoparticles supported on Co_3O_4. Energy 2019; 180: 702-713. https://doi.org/10.1016/j.energy.2019.04.196

[40] Shih YJ, Su CC, Huang YH, Lu MC. SiO_2-supported ferromagnetic catalysts for hydrogen generation from alkaline $NaBH_4$ (sodium borohydride) solution. Energy 2013; 54: 263-270. https://doi.org/10.1016/j.energy.2013.01.063

[41] Duman S, Kaya B, Caf F, Enez B, Fincan SA. Innovative hydrogen release from sodium borohydride hydrolysis using biocatalyst-like Fe_2O_3 nanoparticles impregnated on Bacillus simplex bacteria. International Journal of Hydrogen Energy 2021 ;46 (29): 15410-15430. https://doi.org/10.1016/j.ijhydene.2021.02.028

[42] Li Y, Zhang Q, Zhang N, Zhu L, Zheng J et al. Ru–RuO_2/C as an efficient catalyst for the sodium borohydride hydrolysis to hydrogen. International Journal of Hydrogen Energy 2013; 38 (30): 13360-13367. https://doi.org/10.1016/j.ijhydene.2013.07.071

[43] Zhou S, Yang Q, Liu Y, Cheng L, Isimjan TT et al. Electronic metal-support interactions for defect-induced Ru/Co-Sm2O3 mesosphere to achieve efficient $NaBH_4$ hydrolysis activity. Journal of Catalysis 2024; 433: 115491. https://doi.org/10.1016/j.jcat.2024.115491

[44] Fiorenza R, Scirè S, Venezia AM. Carbon supported bimetallic Ru-Co catalysts for H_2 production through $NaBH_4$ and NH_3BH_3 hydrolysis. International Journal of Energy Research 2018 ;42 (3): 1183-1195. https://doi.org/10.1002/er.3918

[45] Ding XL, Yuan X, Jia C, Ma ZF. Hydrogen generation from catalytic hydrolysis of sodium borohydride solution using Cobalt–Copper–Boride (Co–Cu–B) catalysts. International Journal of Hydrogen Energy 2010; 35 (20): 11077-11084. https://doi.org/10.1016/j.ijhydene.2010.07.030

[46] Tuan TN, Yi Y, Lee JK, Lee J. Fe–B catalyst fabricated by hybrid capacitive adsorption–chemical reduction method and its application for hydrogen production from $NaBH_4$ solution. Catalysis Today 2013; 216: 240-245. https://doi.org/10.1016/j.cattod.2013.05.024

[47] Tuan DD, Lin KYA. Ruthenium supported on ZIF-67 as an enhanced catalyst for hydrogen generation from hydrolysis of sodium borohydride. Chemical Engineering Journal 2018; 351: 48-55. https://doi.org/10.1016/j.cej.2018.06.082

[48] Tran DT, Van HT, Nguyen LH, Quang NV, Tsai YC et al. Hierarchical porous cobalt nanoparticles encapsulated in heteroatom-doped hollow carbon as an enhancing multifunctional catalyst for hydrolysis of sodium borohydride and hydrogenation of bromate in water. Surfaces and Interfaces 2024; 48: 104329. https://doi.org/10.1016/j.surfin.2024.104329

[49] Hao S, Yang L, Cui L, Lu W, Yang Y et al. Self-supported spinel $FeCo_2O_4$ nanowire array: an efficient non-noble-metal catalyst for the hydrolysis of $NaBH_4$ toward on-demand hydrogen generation. Nanotechnology 2016; 27 (46): 46LT03. https://doi.org/10.1088/0957-4484/27/46/46LT03

[50] Patil KN, Prasad D, Bhagyashree, Manoorkar VK, Nabgan W et al. Engineered nano-foam of tri-metallic (FeCuCo) oxide catalyst for enhanced hydrogen generation via $NaBH_4$ hydrolysis. Chemosphere 2021; 281: 130988. https://doi.org/10.1016/j.chemosphere.2021.130988

[51] Zhang H, Xu G, Zhang L, Wang W, Miao W et al. Ultrafine cobalt nanoparticles supported on carbon nanospheres for hydrolysis of sodium borohydride. Renewable Energy 2020; 162: 345-354. https://doi.org/10.1016/j.renene.2020.08.031